Check for updates

Spectroscopic investigations of a pharmaceutical solid form analogue: pyrimethanil L-tartaric acid hemi-cocrystal

Ramandeep S. Dosanjh,[a] Adam Patterson,[b] Joe Harris,[c] Claire Wilson, [ID][a] Matthias J. Gutmann,[d] Paul Collier,[e] Timothy Johnson, [ID][e] Timothy Hyde,[e] Andrew P. E. York,[e] Stewart F. Parker [ID][d] and David Lennon [ID]*[a]

An approach towards pharmaceutical cocrystal analysis is reported for a model cocrystal system of pyrimethanil (an anilinopyrimidine fungicide) and L-tartaric acid (PYL-LTA-CC). Single crystal diffraction studies (X-ray and neutron) show PYL-LTA-CC to crystallise in the primitive orthorhombic space group $P2_12_12$, with the asymmetric unit (1:0.5 stoichiometry) comprising two symmetry independent heterosynthons of pyrimethanil and a half tartaric acid fragment. The neutron diffraction study provides details of the hydrogen bonding in the two adducts and indicates that they are linked by N–H···O and N···H···O hydrogen bonds. Periodic-density functional theory calculations inform on the vibrational properties of PYL-LTA-CC, with the *ab initio* treatment validated by agreement between simulated and experimental inelastic neutron scattering spectra. Fourier transform infrared spectroscopy in attenuated total reflection mode (FTIR-ATR) and Fourier-transform Raman spectroscopy are used to probe the cocrystal's vibrational transitions. Notable deviations between computed and experimental infrared features are observed at higher wavenumbers, reflecting anharmonic contributions within the hydrogen-bonded network. Although most of the vibrational modes in the FTIR-ATR spectrum provide little direct information on the key hydrogen bonding interactions, a set of deformation modes in the range 1668–1618 cm^{-1} are diagnostic of distinct hydrogen bonding interactions within the asymmetric unit. The suitability of Raman spectroscopy for identifying hydrogen bonding is also examined, this technique being less information-rich than FTIR-ATR. Collectively, the study demonstrates how vibrational spectroscopy could be used to supplement investigations on the structure and form of the cocrystal as a potential drug delivery vector for this fungicide.

1. Introduction

Recent years have seen a notable upward trend in interest related to the study and implementation of cocrystals as suitable drug delivery vectors within the pharmaceutical industry.[1–3] This heightened awareness is motivated by a necessity to address challenges associated with improving the physicochemical properties (*i.e.*, solubility, stability, and bioavailability) of active pharmaceutical ingredients (APIs) through the formation of multicomponent crystalline materials using coformer compounds.[4,5] This significance emanates from the establishment of precise, directional hydrogen bonding interactions established between the API and the coformer species during co-crystallisation. In this respect, hydrogen bonding assumes a pivotal role, exerting a profound impact on the design and characteristics of the crystalline entities, influencing the supramolecular architecture and, consequently, the physicochemical properties of an API.[6] Understanding and harnessing the nuances of hydrogen bonding in pharmaceutical cocrystals is essential for tailoring their behaviour, stability, and therapeutic performance, underscoring the strategic importance of these intermolecular forces in pharmaceutical solid-state chemistry.[7]

Determining the crystal structure of relatively complex materials, such as cocrystals, from powder X-ray diffraction data is challenging. Single crystal X-ray diffraction (SCXRD) requires the growth of suitably sized single crystals, which may be time-consuming, with larger crystals still required for neutron diffraction studies. Although low temperature SCXRD can

[a] *School of Chemistry, Joseph Black Building, University of Glasgow, Glasgow G12 8QQ, UK. E-mail: David.Lennon@glasgow.ac.uk; Tel: +44-141-330-4372*

[b] *Veranova, 250 Cambridge Science Park, Cambridge CB4 0WE, UK*

[c] *GlaxoSmithKline, Hills Road, Cambridge CB2 0QQ, UK*

[d] *ISIS Neutron and Muon Facility, STFC Rutherford Appleton Laboratory, Harwell Campus, Didcot OX11 0QX, UK*

[e] *Johnson Matthey Technology Centre, Sonning Common, Reading RG4 9NH, UK*

potentially provide reliable hydrogen atom positions, single crystal neutron diffraction (SCND) provides more accurate hydrogen positions.[8] Attempts at bolstering diffraction data using techniques such as solid-state nuclear magnetic resonance (ss-NMR),[9–11] and X-ray photoelectron spectroscopy (XPS)[12–14] have assisted in rationalising the nature of the bonding with pharmaceutical cocrystals. However, preparation of samples suitable for study by these techniques is not always readily achievable.

As the pharmaceutical industry embraces high throughput screening methods for drug discovery and formulation optimisation,[15] the integration of analytical techniques such as Fourier transform infrared spectroscopy (FTIR) becomes increasingly relevant.[16] In the study of pharmaceutical cocrystals, empirical studies utilising FTIR spectroscopy have been used to monitor spectral changes in functional group frequencies and broadening intensities relative to corresponding moieties in the API and coformer on various cocrystalline systems of pharmaceutical relevance.[17–27] Moreover, attempts have been made at formalising the identification of synthon motifs using model cocrystal systems,[28] and isotopic substitution.[29,30] Nevertheless, the analysis of FTIR spectra of co-crystalline systems is non-trivial, making the assignment of specific structural and the critical hydrogen bonding modes a challenging concept.

The application of predictive, *ab initio*, methods such as Density Functional Theory (DFT) play a pivotal complementary role in enhancing accurate interpretations of experimental vibrational modes.[31] In this regard, several studies have been undertaken that rationalise the FTIR spectra of pharmaceutical cocrystals through the application of discrete DFT optimisation and frequency calculations.[23,25–27,32,33] Acknowledging the significance of precisely portraying long-range intermolecular interactions is paramount in the investigation of hydrogen bonding. Isolated molecule DFT calculations, whilst a valuable approach, are faced with constraints arising from computational complexities, finite basis sets, inadequate treatment of dispersion forces, and the absence of treatment of three-dimensional periodicity by the applied wavefunction.[34] Consequently, a holistic approach based on the complete unit cell becomes imperative for a more comprehensive modelling of the solid-state hydrogen bonding landscape. Advances in electronic structure theory and computational capabilities have led to a rapid proliferation of periodic-DFT (p-DFT) codes that enable calculation of solid-state vibrational frequencies,[35,36] including for pharmaceuticals.[37–41] These software packages incorporate periodic boundary conditions, pseudopotentials, plane-wave basis sets, symmetry operators and dispersion-corrected functionals, enabling a holistic *ab initio* approach based on the complete unit cell, allowing for an accurate representation of intermolecular interactions.[42] Whilst the use of complementary p-DFT and low-frequency terahertz and Raman spectroscopy[43,44] applied to the study of pharmaceutical cocrystals have been reported, along with a number of studies using p-DFT and ss-NMR,[11,45,46] there remains a noticeable gap in contemporary demonstrations of FTIR spectroscopy for the study of pharmaceutical cocrystals.
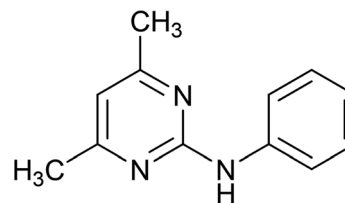

Fig. 1   The chemical structure of pyrimethanil.

This communication employs pyrimethanil as a representative API analogue to assert the applicability of mid-IR spectroscopy, specifically Fourier transform infrared spectroscopy in attenuated total reflection mode (FTIR-ATR), for studying hydrogen bonding motifs present in the crystal structure of a representative cocrystal. Pyrimethanil (4,6-dimethyl-*N*-phenylpyrimidin-2-amine, $C_{12}H_{13}N_3$) (Fig. 1), an anilino-pyrimidine fungicide,[47,48] has gained significant attention due to its structural versatility and ionisable centres, which make it a suitable generic analogue for APIs. Numerous studies have explored the structural and functional roles of pyrimethanil in various formulations, leading to the development of several salts and cocrystals.[49–52] A notable example is the production of Fabran,[53,54] a commercially available agrochemical cocrystal composed of a 1:1 ratio of pyrimethanil and diathianon ($C_{14}H_4N_2O_2S_2$). This communiucation examines a cocrystal of pyrimethanil, specifically pyrimethanil L-tartaric acid hemicocrystal (PYL-LTA-CC), which is formed by combining pyrimethanil with L-tartaric acid ($HO_2CCH(OH)CH(OH)CO_2H$).

A stage-gated approach is adopted herewith: (i) a combination of single crystal X-ray diffraction (SCXRD) and single crystal neutron diffraction (SCND) data identify the relevant hydrogen bonding synthon as defined by graph set notation, (see SI, Section S1);[55,56] (ii) the crystallographic model from the 10 K SCND study is used as a model for p-DFT calculations to predict the vibrational properties of PYL-LTA-CC; (iii) p-DFT calculation outputs are compared to the experimentally obtained inelastic neutron scattering (INS) spectrum;[57] and on validation *via* the INS spectrum, (iv) a complete vibrational analysis for PYL-LTA-CC is performed by application of animation software applied to discrete calculated vibrational transitions. This latter action then enables rationalisation of differences pertaining to hydrogen bonding vibrations in the experimental FTIR-ATR and Raman spectra to be explored. In this way, the study considers the potential of vibrational spectroscopy as an analytical probe in the structural characterisation of this representative pharmaceutical cocrystal.

2. Experimental

PYL-LTA-CC was synthesised by dissolving pyrimethanil (40 mg, 0.2 mmol) in either MeOH (0.8 mL, 20 volumes) or IPA (1.6 mL, 40 volumes) at room temperature, followed by the addition of L-tartaric acid (0.1 mL, 0.1 mmol, 1 mol dm^{-3} stock solution in THF). The solution was then cooled to 5 °C. The resulting suspension was filtered *via* Buchner filtration to yield off-white cubic crystals.

PYL-LTA-CC was characterised by a combination of elemental and thermal analysis, and its structural attributes were then investigated by a combination of single crystal X-ray and neutron diffraction. Crystallographic information has been deposited with the CCDC,[58] under the following repository numbers: CCDC 2385128 for X-ray diffraction and CCDC 2385127 for neutron diffraction. Details of these procedures are outlined in Sections 2.1 and 2.2 of the SI Section. Based on the neutron diffraction data, periodic density functional theory (p-DFT) calculations were used to simulate inelastic neutron scattering (INS), infrared (IR) and Raman spectra, which were compared against experimentally measured spectra. Details of these procedures are outlined in Sections 2.3 and 2.4 of the SI section. Analysis of the vibrational modes obtained in the p-DFT calculations enabled assignments of the vibrational modes of PYL-LTA-CC to be determined. Following convention, infrared spectra are presented from high to low wavenumber, whilst the Raman and INS spectra are plotted from low to high wavenumber.

3. Results & discussion

3.1. Elemental analysis and thermal analysis

Elemental analysis of PYL-LTA-CC confirms a 2 : 1 ratio of pyrimethanil to L-tartaric acid (Table S2). DSC analysis indicates a sharp melting point at *ca.* 140 °C, corroborated by a mean value of 142 °C recorded *via* melting point apparatus (Fig. S4). The absence of additional thermal events suggests that PYL-LTA-CC co-crystallised without polymorphic impurities. TGA supports these findings, showing a single-step decomposition curve with no phase transitions prior to thermal degradation (Fig. S5). These results confirm the sample's purity and stability, providing a foundation for the crystallographic analysis.

3.2. Crystallographic analysis

PYL-LTA-CC crystallises in the orthorhombic space group $P2_12_12$ with $Z = 4$, as confirmed by SCXRD and SCND performed at 150 K and 10 K respectively. Crystallographic details related to the single-crystal diffraction studies of PYL-LTA-CC demonstrate consistent agreement on refined heavy atom positions and geometries and are summarised in the SI, Table S3. The asymmetric unit contains two symmetry-independent pyrimethanil molecules, each hydrogen bonded to half a symmetry-independent half L-tartaric acid fragment, forming two distinct $R_2^2(8)$ diamine-carboxylic acid heterosynthons, designated as $R_2^2(8) > a < b$ and $R_2^2(8) > d > e$ (Fig. 2 and 3).

Each $R_2^2(8)$ synthon features a localised N–H···O hydrogen-bond between the bridging sp^3-hybridised NH moiety of pyrimethanil and the terminal C=O group of the L-tartaric acid fragment. A second interaction occurs between the sp^2-hybridised pyrimidine nitrogen atoms (N2A and N2B) and the terminal O–H group of the L-tartaric acid fragment. SCXRD analysis of the N2A···O2A and N2B···O1B hydrogen bonds revealed ambiguity in the hydrogen atom localisation. Fourier difference maps (Fig. 2a and b), modelled with two partially

occupied hydrogen positions, show diffuse maxima along the N···O axis. This suggests the hydrogen may reside either on the hydroxyl group (neutral synthon) or on the pyrimidine nitrogen (charge-assisted synthon). The associated large thermal ellipsoids, combined with hydrogen's weak X-ray scattering, illustrate the limitations of SCXRD for precise hydrogen localisation. Alternatively, a single, partially delocalised hydrogen position between donor and acceptor atoms may reflect a dynamic equilibrium, indicative of a salt–cocrystal continuum (Fig. S6). These observations in the SCXRD data highlight the need for further examination to define the nature of these bonds more precisely.

Neutron diffraction provides enhanced sensitivity to hydrogen atoms because the scattering power depends on the neutron scattering cross-section, not the number of electrons as for X-ray scattering. H, C, N, and O have similar cross sections so all contribute approximately equally to the scattered intensity enabling more precise localisation of hydrogen atom positions. For PYL-LTA-CC, SCND was performed at 10 K. The nuclear density map of the N2B···O1B hydrogen atoms is characterised by a well-defined single trough, indicating a strong, localised interaction (Fig. 2c). In contrast, the N2A···O2A hydrogen bond (Fig. 2d) exhibits a symmetrical double minimum, equidistant from the donor and acceptor atoms. These features suggest that N2B···O1B corresponds to a neutral hydrogen bond, while the N2A···O2A represented an equidistant hydrogen bonding continuum.

Bond geometry analysis provides further insight (Table S4). The H···A distances are 1.323 Å (N2A···O2A) and 1.381 Å (N2B···O1B), while the corresponding D···A distances are 2.604 Å (N2A···O2A) and 2.648 Å (N2B···O1B) respectively. Although these are small differences they demonstrate the hydrogen bonds have different character. The close correspondence between SCND- and SCXRD-derived geometries, with minimal differences in bond lengths and angles, for the non-hydrogen atoms supports the proposition that there is a distinct difference between the two hydrogen bonds. The integration of SCND and SCXRD data exemplifies the complementary nature of these techniques: SCND resolves positional ambiguities, while SCXRD is more accessible but still provides consistent geometric parameters. Together, they offer a cohesive structural basis for subsequent computational and vibrational analyses.

3.3. Vibrational mode analysis of PYL-LTA-CC

The p-DFT calculations to predict vibrational properties of PYL-LTA-CC in this study have been based on the SCND-derived structure, due to the precise localisation of hydrogen atoms. Although the hydrogen positions of PYL-LTA-CC are more precisely located by neutron diffraction data, X-ray data is generally sufficiently close that it can be used as input for a periodic DFT calculation.

PYL-LTA-CC contains 288 atoms with 864 degrees of freedom. With respect to the correlation method of vibrational spectroscopy,[59,60] the $P2_12_12$ crystal system of PYL-LTA-CC can be represented by the D_2 symmetry point group (Table S5).
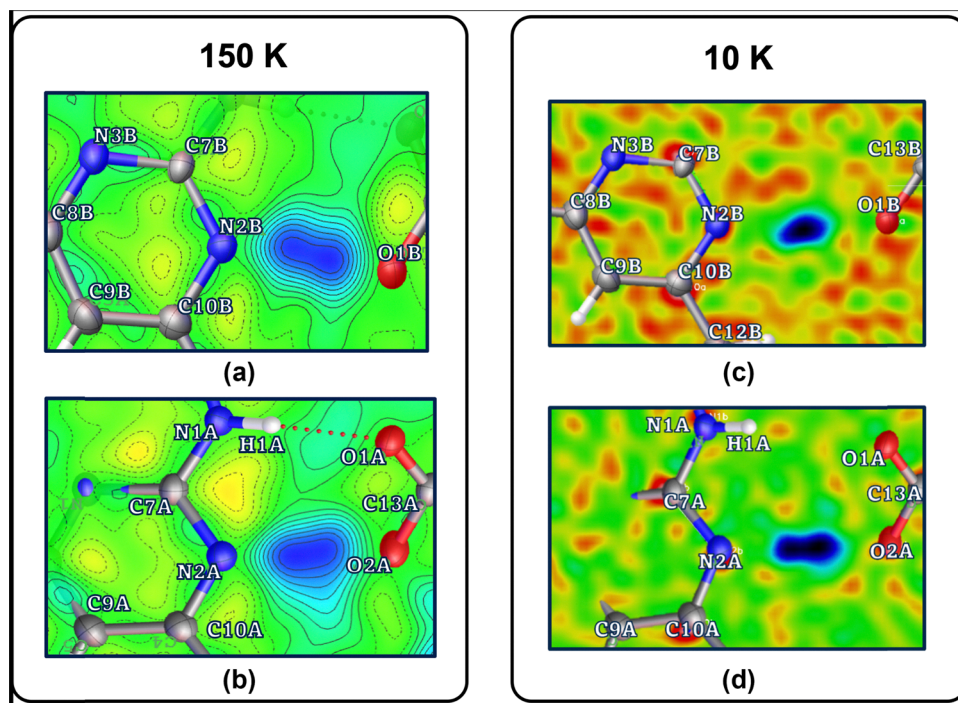
24768 | *Phys. Chem. Chem. Phys.*, 2025, **27**, 24766–24776

This journal is © the Owner Societies 2025

Fig. 2 X-ray Fourier difference maps of the (a) N2B···O1B and (b) N2A···O2A hydrogen-bonds produced at 150 K and neutronic Fourier difference maps of the (c) N2B···O1B and (d) N2A···O2A hydrogen-bonds produced at 10 K.

The number of normal modes can then be represented by the following set of irreducible representations:

$$\Gamma_{vib} = 216A + 214B_1 + 214B_2 + 214B_3.$$

Under D_2 symmetry, A modes are Raman-active and B_1, B_2 and B_3 modes are both Raman and IR-active. A comprehensive vibrational assignment of PYL-LTA-CC spanning the range of 400–4000 cm^{-1} is provided in the SI, Table S6.

3.4. INS validation of p-DFT calculations for PYL-LTA-CC

The phonon dataset generated from the p-DFT calculation was used to simulate the INS spectrum of PYL-LTA-CC and compared with experimental data collected on the TOSCA INS spectrometer. The experimental spectrum is optimal in the region of 400–1800 cm^{-1},[61] and accordingly, the comparison was restricted to this region. Simulated and experimental INS spectra are shown in Fig. 4, where their close agreement validates the p-DFT outcomes, and provides a route to vibrational mode assignments.

The intense bands in the experimental INS spectrum reflect vibrational modes, that involve significant hydrogen motion. These bands arise from aromatic (phenyl and pyrimidine) ring deformations, L-tartaric acid backbone motions, and C–H and O–H bending and torsional modes. Several distinct features are assigned to hydrogen-bonding deformations, which are key to probing the nature of the interactions within the two $R_2^2(8)$ heterosynthons. Features at 841 and 982 cm^{-1} are assigned to the out-of-plane δ(N1B–H1BA···O2B) hydrogen-bonding deformation and the out-of-plane δ(N1A–H1A···O1A) deformation

respectively. A medium-intensity band at 1118 cm^{-1} is attributed to out-of-plane δ(N2A–H2A···O2A) and δ(N2B···H1B···O1B) deformation modes. The highest-frequency band, observed as a broad feature at 1666 cm^{-1}, is assigned to in-phase and out-of-phase bending vibrations involving the N–H···O and N···H···O hydrogen bonds associated with the $R_2^2(8)$ motifs.

3.5. FTIR-ATR Analysis of PYL-LTA-CC

The FTIR-ATR spectrum lays the groundwork for further discussion regarding identification of synthon-specific hydrogen bonding vibrational modes. Good agreement between the experimental and simulated spectra is observed in the fingerprint region (1800–400 cm^{-1}, Fig. 5a), while increasing deviations in the higher-wavenumber stretching region (4000–1800 cm^{-1}, Fig. 5b) are informative concerning the nature of the hydrogen bonds (Fig. S7). In addition to these hydrogen-bonding modes, several other well-resolved bands in the fingerprint region are evident, corresponding to phenyl and pyridine ring deformations, C–O stretching, and methyl group vibrations.

Concentrating first on the fingerprint region of the IR spectrum (Fig. 5a), the medium intensity feature at 1112 cm^{-1} arises from out-of-plane bending vibrations associated with the N2A···H2A···O2A and N2B···H1B···O1B hydrogen bonds. Additional out-of-plane deformation modes associated with the N1A–H1A···O1A and N1B–H1BA···O2B hydrogen bonds were identified in the simulated spectra at 995 and 854 cm^{-1}, respectively. However, in the experimental FTIR-ATR spectrum, these appear as a weak band at 841 cm^{-1} and a poorly resolved shoulder at 1013 cm^{-1}, making their confident experimental assignment challenging.

This journal is © the Owner Societies 2025

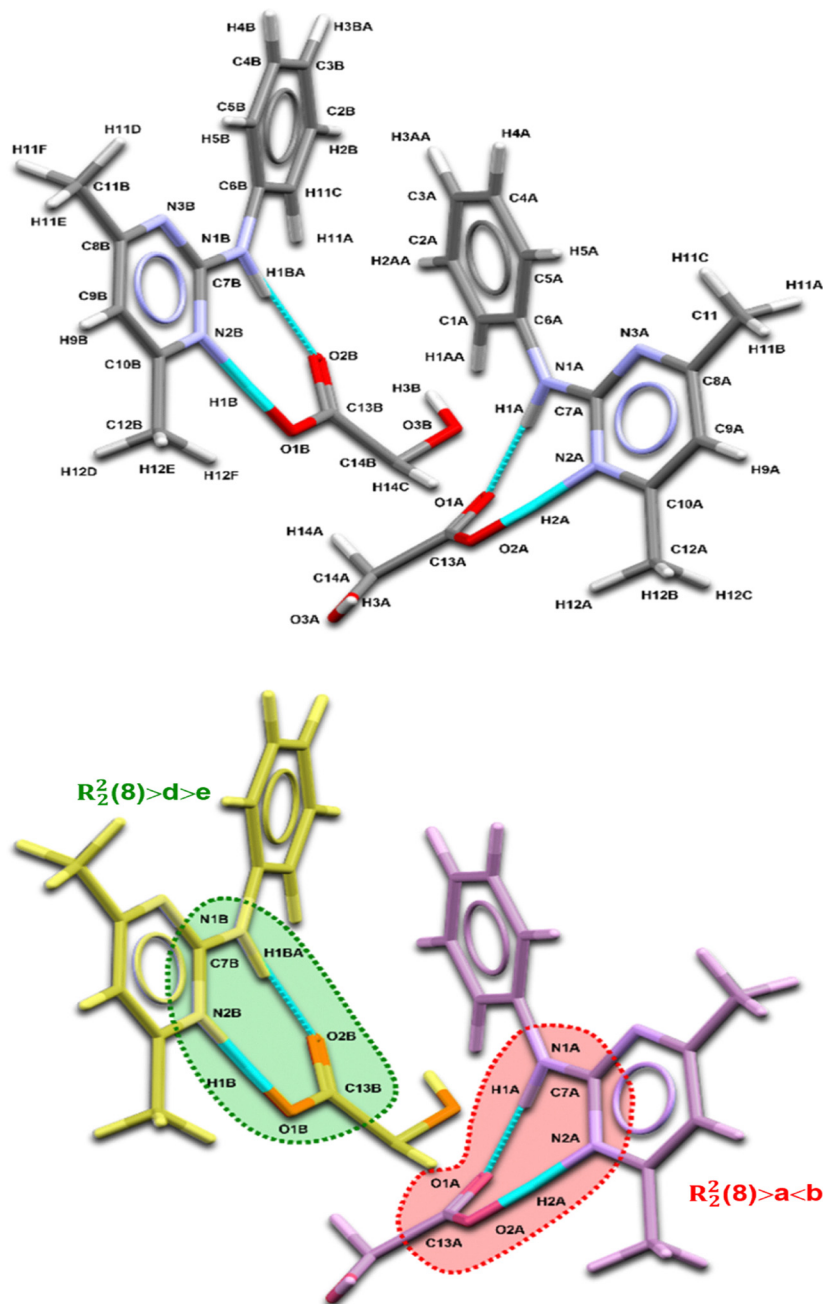*Phys. Chem. Chem. Phys.*, 2025, **27**, 24766–24776 | **24769**

Fig. 3 (a) The labelled asymmetric unit of PYL-LTA-CC as determined from SCND at 10 K, showing the atomic numbering system used throughout the vibrational analysis to identify specific atoms in vibrational mode assignments. (b) The asymmetric unit of PYL-LTA-CC is coloured and annotated to represent the different symmetry independence species and hydrogen-bonding motifs. The symmetry independent $R_2^2(8)$ heterosynthons are coloured yellow and magenta. The $R_2^2(8) > d > e$ synthon is encircled in green, whilst the $R_2^2(8) > a < b$ synthon is encircled in red. Hydrogen-bonding interactions are shown in turquoise. Atoms involved in hydrogen-bonding are labelled accordingly.

In the low-resolution simulation (Fig. 5a, blue trace), a single band at 1644 cm^{-1} corresponds to a convolution of in-phase and out-of-phase δ(N–H$\cdots$O) and δ(N$\cdots$H$\cdots$O) in-plane bending modes. The high-resolution simulation (Fig. 5a, green trace) reveals this band to arise from four distinct hydrogen-bond deformation modes: the out-of-phase δ(N1B–H1BA$\cdots$O2B) and δ(N2B$\cdots$H1B$\cdots$O1B) vibrations at 1621 cm^{-1}; their in-phase counterparts at 1641 cm^{-1}; the in-phase δ(N1A–H1A$\cdots$O1A) and δ(N2A$\cdots$H2A$\cdots$O2A) modes at 1657 cm^{-1}; and the

corresponding out-of-phase modes at 1668 cm^{-1}. These predicted features can be mapped onto the experimental FTIR-ATR spectrum: the out-of-phase δ(N1B–H1BA$\cdots$O2B) and δ(N2B$\cdots$H1B$\cdots$O1B) modes correspond to a broad shoulder at 1618 cm^{-1}, while the in-phase counterparts are assigned to a broader band centred at 1636 cm^{-1}. The δ(N1A–H1A$\cdots$O1A) and δ(N2A$\cdots$H2A$\cdots$O2A) modes (both in-phase and out-of-phase) are assigned to a broad feature at 1665 cm^{-1}. This fine resolution of H-bond-associated deformation modes highlights
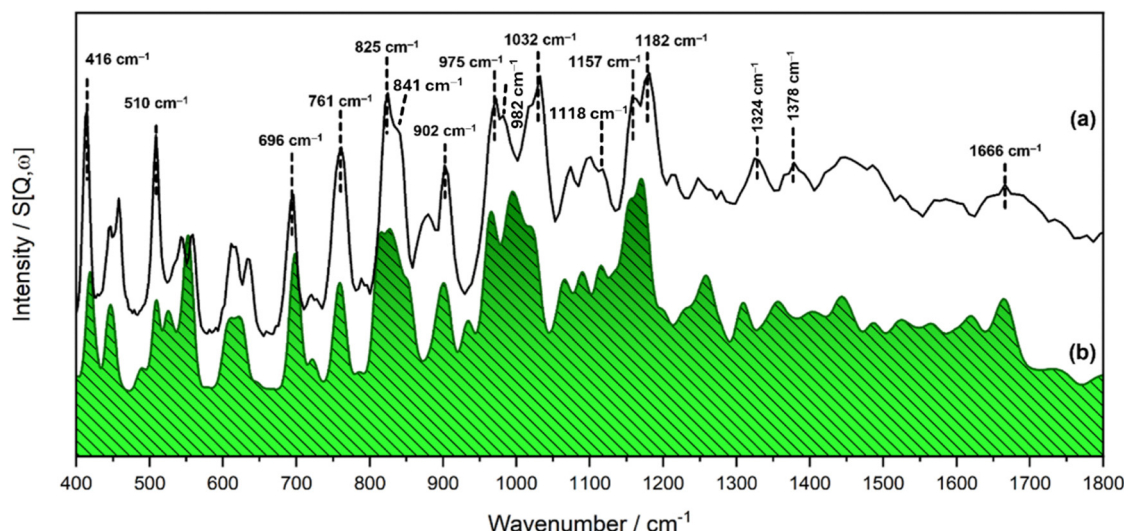
24770 | *Phys. Chem. Chem. Phys.*, 2025, **27**, 24766–24776

This journal is © the Owner Societies 2025

Fig. 4 (a) Experimental and (b) simulated INS spectra in the range 400–1800 cm^{-1} of PYL-LTA-CC.

the capability of FTIR-ATR spectroscopy, when combined with high-resolution simulation, to distinguish multiple hydrogen-bonding motifs within complex salt–cocrystal systems. With reference to Fig. 5a, contributions from features at 1618, 1636 and 1665 cm^{-1} are discernible in the experimental spectrum.

On comparing the experimental and simulated FTIR-ATR C–H/N–H/O–H stretching region, (Fig. 5b) the simulated spectrum is shown to be dominated by four intense bands, which are assigned to the stretching modes of the hydrogen bonding associated with the $R_2^2(8)$ heterosynthons. Simulated bands at 1990 and 3170 cm^{-1} correspond to the v(N2B···H1B···O1B) and the v(N1B–H1B···O2B) stretching modes in the $R_2^2(8) > d > e$ synthon respectively. The $R_2^2(8) > a < b$ synthon is represented by the simulated peak at 2244 cm^{-1}, (v(N2A···H2A···O2A)), whilst the predicted band at 2779 cm^{-1} corresponds to v(N1A–H1A···O1A). The broadening of these modes in the experimental IR spectrum complicates direct mapping of simulated vibrations across this region.

The marked difference between the observed and calculated infrared spectra in the OH stretch region are a common feature of DFT calculations.[62–65] Most DFT calculations (including these reported here, Fig. 5b) use the harmonic approximation. For covalent bonds this is entirely reasonable, as shown by the good agreement in Fig. 4 and 5a. For hydrogen bonded systems, the approximation becomes progressively poorer as the hydrogen bond strength increases. For PYL-LTA-CC, Fig. 2 shows that there are two types of hydrogen bond present, one of which is a double well potential, so the potential energy wells will not be accurately described by a harmonic potential, so poor agreement is to be expected for the O–H stretch modes.

The origin of the extreme broadening of the vibrations of hydrogen bonded systems seen in the infrared spectra has been long debated and a number of causes have been suggested. These include increased anharmonicity in the O–H stretch,[66,67] coupling with low energy vibrations[68] and electrical anharmonicity.[69] There are computational methods to address

each of these effects,[70–72] however, the computational cost rapidly becomes prohibitive and such methods are beyond our present resources.

Regardless of the origins, this complexity significantly compromises direct corroboration between experimental and simulated stretching modes. A shown in Fig. 5(b), broadening also affects aromatic and alkyl C–H bonds grouped between 2969–3099 cm^{-1}. Nevertheless, two simulated peaks at 3444 cm^{-1} and 3530 cm^{-1}, corresponding to v(O3B–H3B) and v(O3A–H3A) are both represented in the experimental spectrum by a broad but, nonetheless, defined peak at 3490 cm^{-1}. Although some studies have implemented anharmonic corrections for small semi-rigid molecules,[69] such methods remain computationally prohibitive for pharmaceutically relevant systems.[70] In this manner, further computational refinement of PYL-LTA-CC is beyond the scope of the present study.

3.6. FT-Raman spectroscopy

Fig. 6 presents the FT-Raman spectrum of PYL-LTA-CC recorded over the range 400–4000 cm^{-1}. The spectrum displays distinct vibrational features associated with the pyrimidine and monosubstituted benzene ring systems, methyl C–H stretches, and characteristic modes of the L-tartaric acid fragments. In certain cases, the experimental dataset enables resolution of deformation modes related to hydrogen bonding. However, the absence of simulated FT-Raman spectra precludes more definitive characterisation of some coupled or overlapping modes.

The most intense band in the spectrum is observed at 998 cm^{-1}, comprising overlapping contributions from $\mathcal{M}_9(a_1)$ and $\mathcal{M}_{15}(b_1)$ in-plane symmetric stretching modes, symmetric pyrimidine ring stretching within the $R_2^2(8) > d > e$ heterosynthon, and the out-of-plane δ(N1A–H1A···O1A) mode. However, due to the strong overlap of multiple vibrational modes in this region, this hydrogen bonding contribution cannot be isolated, and is therefore not independently diagnostic. Two additional weak features observed at 841 cm^{-1} and 1112 cm^{-1}

This journal is © the Owner Societies 2025

Phys. Chem. Chem. Phys., 2025, **27**, 24766–24776 | **24771**
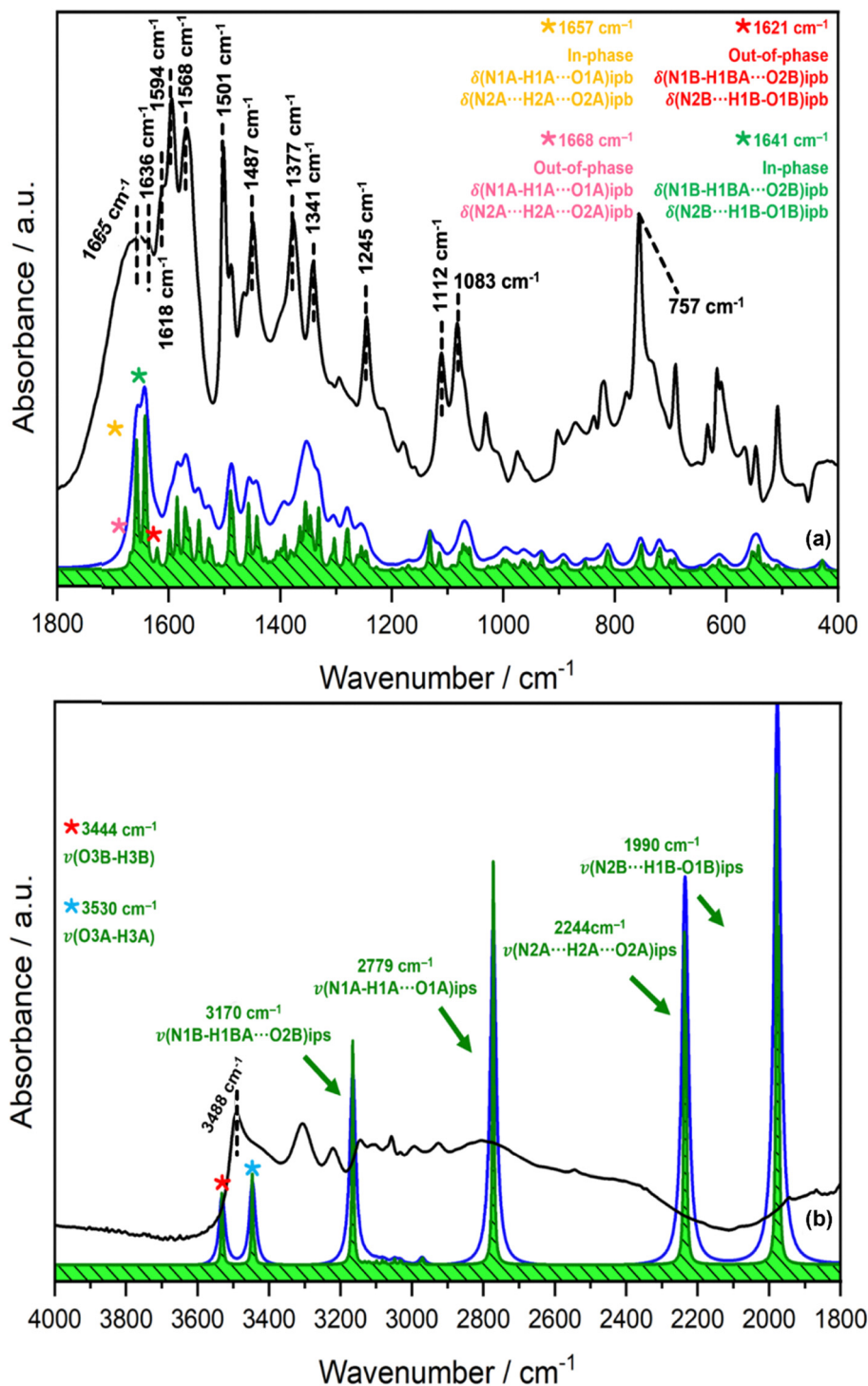
Fig. 5 Experimental (black trace) and simulated FTIR-ATR spectra of PYL-LTA-CC. Simulated spectra are shown at low resolution, (blue trace, 20 cm^{-1}), and high-resolution (green trace, 5 cm^{-1}). (a) Fingerprint region (1800–400 cm^{-1}); (b) Stretching region (4000–1800 cm^{-1}).

correspond to out-of-plane N–H deformation modes. However, the weak feature at 841 cm^{-1} appears as a composite with other overlapping vibrational contributions and, therefore, is not a reliable marker of the hydrogen-bonding in PYL-LTA-CC. The feature at 1112 cm^{-1}, although more spectrally isolated, is too weak a feature to be diagnostically practical.

A weak shoulder at 1618 cm^{-1} is assigned to in-plane hydrogen-bond deformation modes involving the out-of-phase N1B–H1BA···O2B and N2B···H1B···O1B hydrogen bonds. However, the absence of simulated FT-Raman data in this region, or additional coupled hydrogen-bonding bands clearly attributable to isolated hydrogen-bonding vibrations, prevents
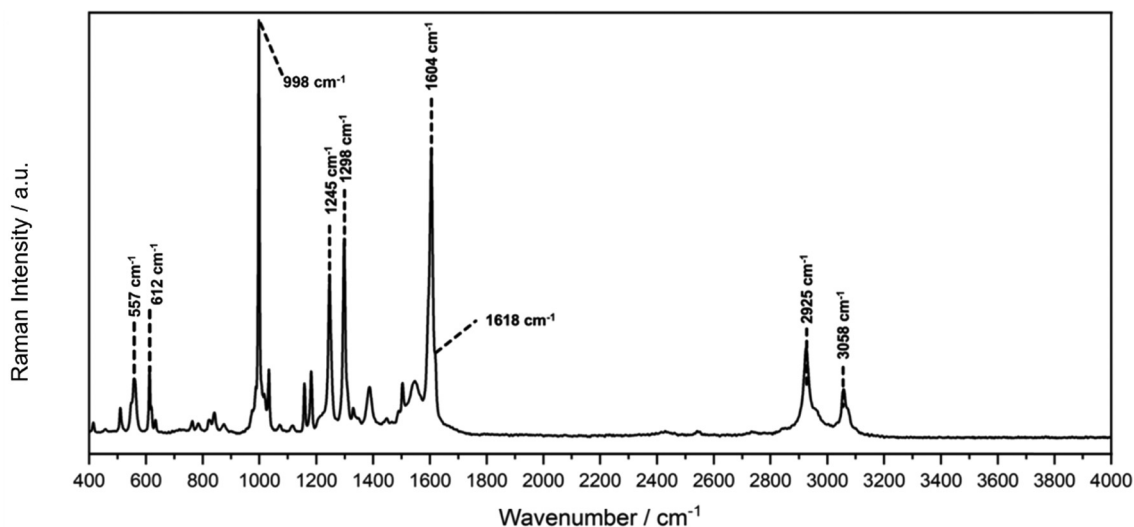
24772 | *Phys. Chem. Chem. Phys.*, 2025, **27**, 24766–24776

This journal is © the Owner Societies 2025

Fig. 6 Experimental FT-Raman spectrum of PYL-LTA-CC in the range 400–4000 cm^{-1}.

further differentiation of $R_2^2(8)$ heterosynthon-related modes, as was possible in the assignment of the INS and, crucially, of the FTIR-ATR spectra of PYL-LTA-CC. In the high-wavenumber region, no Raman-active hydrogen-bond stretching bands or diagnostic synthon-specific signals of sufficient intensity are observed in the FT-Raman spectrum.

4. Conclusions

PYL-LTA-CC is a cocrystal that is representative of an API and coformer structural motif. Moreover, the material is a proxy for new drug delivery vectors that are under development in certain healthcare scenarios.[2] Here, PYL-LTA-CC has been analysed

Table 1 Vibrational assignments of hydrogen bonding features of PYL-LTA-CC. [ip = in-plane bend, op = out-of-plane. vw = very weak, w = weak, m = medium, s = strong, vs = very strong, sh = shoulder, br = broad, v = stretching mode, δ = bending mode]

Approximate description	p-DFT/ cm^{-1}	FTIR-ATR/ cm^{-1}	FT-Raman/ cm^{-1}	INS/cm^{-1}
δ(N1B–H1BA)op	854	841 w	841 w	841 s
δ(N1A–H1A)op	995	1013 sh	998 vs	982 vs
δ(N2A···H2A···O2A)op	1115	1112 s	1112 vw	1118 m
δ(N2B···H1B···O1B)op	1133	1112 s	1112 vw	1118 m
Out-of-phase δ(N1B–H1BA···O2B)ip δ(N2B···H1B···O1B)ip	1621	1618 br	1618 vw	1666 br
In-phase δ(N1B–H1BA···O2B)ip δ(N2B···H1B···O1B)ip	1641	1636 br	—	1666 br
In-phase δ(N1A–H1A···O1A)ip δ(N2A···H2A···O2A)ip	1657	1655 br	—	1666 br
Out-of-phase δ(N1A–H1A···O1A)ip δ(N2A···H2A···O2A)ip	1668	1655 br	—	1666 br
v(N2B···H1B···O1B)	1990	—	—	—
v(N2A···H2A···O2A)	2244	—	—	—
v(N1A–H1A···O1A)	2779	—	—	—
v(N1B–H1BA···O2B)	3169	—	—	—

deploying a number of analytical techniques that include SNCD and SCXRD (Table S3), p-DFT and INS (Fig. 4), FTIR-ATR (Fig. 5) and FT-Raman (Fig. 6). Acknowledging the complexity inherent with Table S6, Table 1 provides a summary of key hydrogen bond specific vibrational modes that help define the structural form of the cocrystal API formulation under consideration. Fig. S8 presents the FTIR-ATR, Raman and INS spectra of PYL-LTS-CC plotted alongside each other in the range 400–4000 cm^{-1} and shows the differences in the corresponding spectral profiles.

Overall, the following conclusions can be drawn.

• The complementary approach of using SCXRD and SCND has defined the spatial arrangement of both the atoms of the overall molecular scaffold and the nature of the hydrogen bonding within the crystal system (Table S3). The SCND-refined unit cell was selected as the structural model for subsequent p-DFT calculations, owing to its superior precision in localising hydrogen atom positions.

• The experimental INS spectrum is well matched by the simulated INS spectrum derived from p-DFT calculations based on the SCND-refined structure (Fig. 4). This validation of the structural model enables reliable simulation of infrared and Raman spectra, with visual animations of the calculated optical modes facilitating assignments of vibrational transitions in the experimental vibrational spectra.

• The inherent sensitivity of INS to hydrogenous vibrational motions enabled the assignment of in-plane and out-of-plane hydrogen-bonding deformation modes associated with the $R_2^2(8)$ heterosynthons, providing a valuable reference for further analysis of optical vibrational spectra.

• The fingerprint region of the experimental FTIR-ATR spectrum (Fig. 5a) shows good agreement with the p-DFT simulated spectrum, enabling the identification of several structural and hydrogen-bonding deformation modes associated with the $R_2^2(8)$ heterosynthons (e.g. out-of-plane bending modes associated with the N2A···H2A···O2A and N2B···H1B···O1B hydrogen bonds at 1112 cm^{-1}). Moreover, four coupled

This journal is © the Owner Societies 2025

Phys. Chem. Chem. Phys., 2025, **27**, 24766–24776 | **24773**

in-plane hydrogen-bonding deformation modes were observed as broadened bands centred at approximately 1618, 1636, and 1665 cm^{-1}.

• In the C–H/O–H/N–H stretching region of the FTIR-ATR spectrum, (Fig. 5b), there is very poor agreement between experiment and theory. As is common with hydrogen-bonded systems, the experimental data exhibits a complex profile extending over 1000 cm^{-1}. This arises from a variety of factors but especially the electrical anharmonicity that is typical of hydrogen bonded systems.

• The FT-Raman spectrum of PYL-LTA-CC (Fig. 6) exhibits clear vibrational features associated with prominent structural elements of the pyrimethanil and L-tartaric acid components. However, the prevalence of spectral overlap and the inherently low intensity of several hydrogen-bonding modes limit its utility for definitive characterisation of hydrogen-bonding interactions within the cocrystal, particularly in comparison to the greater diagnostic capability afforded by the FTIR-ATR spectrum.

Author contributions

Dosanjh: data curation, formal analysis, investigation, methodology, visualization, roles/writing – original draft; Patterson: data curation, validation, visualization; Harris: data curation, validation, visualization; Wilson: methodology, software, validation, formal analysis, investigation, data curation, writing – review & editing; Guttmann: data curation, formal analysis, validation; Collier: conceptualization, funding acquisition, project administration, resources, supervision; Johnson: investigation, project administration, supervision, visualization; Hyde: investigation, project administration, supervision, visualization; York: investigation, project administration, supervision; visualization; Parker: data curation, formal analysis, investigation, methodology, supervision, validation, visualization, writing – review & editing; Lennon: investigation; methodology; project administration; supervision; validation; roles/writing – original draft.

Conflicts of interest

There are no conflicts of interest associated with this article.

Data availability

Data for this article are available from the University of Glasgow Library.

Supplementary information (SI): Section S1, an overview of Graph set notation; Section S2, experimental details; Fig. S1, the INS spectrum of PYL-LTA-CC; Fig. S2. Screenshots from molecular modelling software showing the simulated stretching modes of hydrogen-bonding interactions in the asymmetric unit of PYL-LTA-CC; Fig. S3, vibrational modes of a monosubstituted benzene in C_{2v} symmetry; Table S1, the approximate wavenumber ranges for the $\mathcal{M}_i X$ vibrations; Table S2, elemental analysis of PYL-LTA-CC; Fig. S4, differential scanning calorimetry of PYL-LTA-CC; Fig. S5, thermal gravimetric analysis of PYL-LTA-CC; Table S3, crystallographic data and refinement details for PYL-LTA-CC, obtained from SCXRD measurements at 150 K and SCND measurements at 10 K; Fig. S6, hydrogen-bonding arrangements identified *via* SCXRD for the N···H···O hydrogen bonds in the $R_2^2(8)$ synthons of the asymmetric unit in PYL-LTA-CC; Table S4, hydrogen-bond geometries determined from SCXRD and SCND data refinement; Table S5, character table for the D_2 point group; Table S6, the vibrational assignments of PYL-LTA-CC in the range 4000–400 cm^{-1} Fig. S7, (a) experimental and (b) simulated FTIR-ATR spectra of PYL-LTA-CC (4000–400 cm^{-1}); Fig. S8, vibrational spectra of PYL-LTA-CC (400–4000 cm^{-1}): (a) FTIR-ATR, (b) FT-Raman and (c) INS. See DOI: **https://doi.org/10.1039/d5cp02802g**.

CCDC 2385127 and 2385128 contain the supplementary crystallographic data for this paper.[73a,b]

References

1 A. V. Trask, *Mol. Pharm.*, 2007, **4**, 301–309.
2 Ö. Almarsson, M. L. Peterson and M. Zaworotko, *Pharm. Patent Analyst*, 2012, **1**, 313–327.
3 N. K. Duggirala, M. L. Perry, Ö. Almarsson and M. J. Zaworotko, *Chem. Commun.*, 2016, **52**, 640–655.
4 B. M. Couillaud, P. Espeau, N. Mignet and Y. Corvis, *ChemMedChem*, 2019, **14**, 8–23.
5 S. Kumar and A. Nanda, *Mol. Cryst. Liq. Cryst.*, 2018, **667**, 54–77.
6 S. Bhattacharya, K. S. Peraka and M. J. Zaworotko, in *Monographs in Supramolecular Chemistry*, ed C. B. Aakeröy and A. S. Sinha, Royal Society of Chemistry, Cambridge, 2018, pp. 33–79.
7 A. Erxleben, *Pharmaceutics*, 2020, **12**, 834.
8 C. C. Wilson, *Single Crystal Neutron Diffraction from Molecular Materials*, World Scientific, 2000.
9 D. C. Apperley, R. A. Fletton, R. K. Harris, R. W. Lancaster, S. Tavener and T. L. Threlfall, *J. Pharm. Sci.*, 1999, **88**, 1275–1280.

10 D. Luedeker, R. Gossmann, K. Langer and G. Brunklaus, *Cryst. Growth Des.*, 2016, **16**, 3087–3100.

11 L. Zhao, M. P. Hanrahan, P. Chakravarty, A. G. DiPasquale, L. E. Sirois, K. Nagapudi, J. W. Lubach and A. J. Rossini, *Cryst. Growth Des.*, 2018, **18**, 2588–2601.

12 S. Tothadi, T. R. Shaikh, S. Gupta, R. Dandela, C. P. Vinod and A. K. Nangia, *Cryst. Growth Des.*, 2021, **21**, 735–747.

13 J. S. Stevens, S. J. Byard and S. L. M. Schroeder, *J. Pharm. Sci.*, 2010, **99**, 4453–4457.

14 J. S. Stevens, L. K. Newton, C. Jaye, C. A. Muryn, D. A. Fischer and S. L. M. Schroeder, *Cryst. Growth Des.*, 2015, **15**, 1776–1783.

15 S. L. Morissette, Ö. Almarsson, M. L. Peterson, J. F. Remenar, M. J. Read, A. V. Lemmo, S. Ellis, M. J. Cima and C. R. Gardner, *Adv. Drug Delivery Rev.*, 2004, **56**, 275–300.

16 M. Rodrigues, J. Lopes, A. Guedes, J. Sarraguça and M. Sarraguça, *Spectrochim. Acta, Part A*, 2020, **229**, 117876.

17 S. Basavoju, D. Boström and S. P. Velaga, *Cryst. Growth Des.*, 2006, **6**, 2699–2708.

18 S. Basavoju, D. Boström and S. P. Velaga, *Pharm. Res.*, 2008, **25**, 530–541.

19 H. R. H. Ali, A. Alhalaweh and S. P. Velaga, *Drug Dev. Ind. Pharm.*, 2013, **39**, 625–634.

20 M. R. Shimpi, S. L. Childs, D. Boström and S. P. Velaga, *CrystEngComm*, 2014, **16**, 8984–8993.

21 S. Chakraborty, S. Ganguly and G. R. Desiraju, *CrystEngComm*, 2014, **16**, 4732–4741.

22 J. I. Arenas-García, D. Herrera-Ruiz, K. Mondragón-Vásquez, H. Morales-Rojas and H. Höpfl, *Cryst. Growth Des.*, 2010, **10**, 3732–3742.

23 K. Srivastava, M. R. Shimpi, A. Srivastava, P. Tandon, K. Sinha and S. P. Velaga, *RSC Adv.*, 2016, **6**, 10024–10037.

24 K. Srivastava, E. Khan, M. R. Shimpi, P. Tandon, K. Sinha and S. P. Velaga, *CrystEngComm*, 2018, **20**, 213–222.

25 P. Verma, A. Srivastava, A. Shukla, P. Tandon and M. R. Shimpi, *New J. Chem.*, 2019, **43**, 15956–15967.

26 P. Prajapati, J. Pandey, P. Tandon, K. Sinha and M. R. Shimpi, *Front. Chem.*, 2022, **10**, 848014.

27 J. Pandey, P. Prajapati, M. R. Shimpi, P. Tandon, S. P. Velaga, A. Srivastava and K. Sinha, *RSC Adv.*, 2016, **6**, 74135–74154.

28 A. Mukherjee, S. Tothadi, S. Chakraborty, S. Ganguly and G. R. Desiraju, *CrystEngComm*, 2013, **15**, 4640–4654.

29 Z. Dega-Szafran, G. Dutkiewicz, Z. Kosturkiewicz and M. Szafran, *J. Mol. Struct.*, 2008, **889**, 286–296.

30 K. Iwata, M. Karashima and Y. Ikeda, *Mol. Pharmaceutics*, 2017, **14**, 2350–2358.

31 J. Aaltonen, K. C. Gordon, C. J. Strachan and T. Rades, *Int. J. Pharm.*, 2008, **364**, 159–169.

32 C. C. da Silva, F. F. Guimarães, L. Ribeiro and F. T. Martins, *Spectrochim. Acta, Part A*, 2016, **167**, 89–95.

33 M. Wan, J. Fang, J. Xue, J. Liu, J. Qin, Z. Hong, J. Li and Y. Du, *Int. J. Mol. Sci.*, 2022, **23**, 8550.

34 A. H. Mazurek, L. Szeleszczuk and D. M. Pisklak, *Pharmaceutics*, 2020, **12**, 415.

35 D. V. Nickel, S. P. Delaney, H. Bian, J. Zheng, T. M. Korter and D. M. Mittleman, *J. Phys. Chem. A*, 2014, **118**, 2442–2446.

36 M. P. Davis and T. M. Korter, *Mol. Pharm.*, 2022, **19**, 3385–3393.

37 G. Kresse and J. Furthmüller, *Phys. Rev. B: Condens. Matter Mater. Phys.*, 1996, **54**, 11169–11186.

38 B. Delley, *J. Chem. Phys.*, 2000, **113**, 7756–7764.

39 R. Dovesi, R. Orlando, B. Civalleri, C. Roetti, V. R. Saunders and C. M. Zicovich-Wilson, *Z. Kristallogr. - Cryst. Mater.*, 2005, **220**, 571–573.

40 P. Giannozzi, S. Baroni, N. Bonini, M. Calandra, R. Car, C. Cavazzoni, D. Ceresoli, G. L. Chiarotti, M. Cococcioni, I. Dabo, A. D. Corso, S. de Gironcoli, S. Fabris, G. Fratesi, R. Gebauer, U. Gerstmann, C. Gougoussis, A. Kokalj, M. Lazzeri, L. Martin-Samos, N. Marzari, F. Mauri, R. Mazzarello, S. Paolini, A. Pasquarello, L. Paulatto, C. Sbraccia, S. Scandolo, G. Sclauzero, A. P. Seitsonen, A. Smogunov, P. Umari and R. M. Wentzcovitch, *J. Phys.: Condens. Matter*, 2009, **21**, 395502.

41 S. J. Clark, M. D. Segall, C. J. Pickard, P. J. Hasnip, M. I. J. Probert, K. Refson and M. C. Payne, *Z. Kristallogr. - Cryst. Mater.*, 2005, **220**, 567–570.

42 F. Zhang, H.-W. Wang, K. Tominaga and M. Hayashi, *Wiley Interdiscip. Rev.: Comput. Mol. Sci.*, 2016, **6**, 386–409.

43 S. P. Delaney and T. M. Korter, *J. Phys. Chem. A*, 2015, **119**, 3269–3276.

44 Y. Otsuka, A. Ito, M. Takeuchi, T. Sasaki and H. Tanaka, *J. Drug Delivery Sci. Technol.*, 2020, **56**, 101215.

45 P. Li, Y. Chu, L. Wang, R. M. Wenslow, K. Yu, H. Zhang and Z. Deng, *CrystEngComm*, 2014, **16**, 3141–3147.

46 F. Rossi, P. Cerreia Vioglio, S. Bordignon, V. Giorgio, C. Nervi, E. Priola, R. Gobetto, K. Yazawa and M. R. Chierotti, *Cryst. Growth Des.*, 2018, **18**, 2225–2233.

47 A. Daniels and J. A. Lucas, *Pestic. Sci.*, 1995, **45**, 33–41.

48 C. Yu, T. Zhou, K. Sheng, L. Zeng, C. Ye, T. Yu and X. Zheng, *Int. J. Food Microbiol.*, 2013, **164**, 155–160.

49 M. Wang, H. Lei, Z. Hou and S. Wang, *J. Therm. Anal. Calorim.*, 2013, **114**, 313–319.

50 M. Wang, H. Lei, J. Zhang, Z. Hou, Y. Seki, Y. Sawada and S. Wang, *J. Therm. Anal. Calorim.*, 2014, **117**, 1335–1340.

51 X.-H. Sun, H.-F. Wang, Y.-F. Liu, B. Chen, P.-J. Ji and J.-W. Yang, *Chin. J. Org. Chem.*, 2004, **24**, 506–511.

52 X.-H. Sun, Y.-F. Liu, Z.-C. Tan, Y.-Y. Di, H.-F. Wang and M.-H. Wang, *J. Chem. Thermodyn.*, 2004, **36**, 895–899.

53 M. Viertelhaus and A. Hafner, *Chim. Oggi*, 2015, **33**, 23–26.

54 A.-C. Pöppler, E. K. Corlett, H. Pearce, M. P. Seymour, M. Reid, M. G. Montgomery and S. P. Brown, *Acta Crystallogr., Sect. C: Struct. Chem.*, 2017, **73**, 149–156.

55 M. C. Etter, J. C. MacDonald and J. Bernstein, *Acta Crystallogr., Sect. B: Struct. Sci.*, 1990, **46**, 256–262.

56 M. C. Etter, *Acc. Chem. Res.*, 1990, **23**, 120–126.

57 B. S. Hudson, *J. Phys. Chem. A*, 2001, **105**, 3949–3960.

58 C. R. Groom, I. J. Bruno, M. P. Lightfoot and S. C. Ward, *Acta Crystallogr., Sect. B: Struct. Sci., Cryst. Eng. Mater.*, 2016, **72**, 171–179.

This journal is © the Owner Societies 2025

Phys. Chem. Chem. Phys., 2025, **27**, 24766–24776 | **24775**

59 W. G. Fateley, N. T. McDevitt and F. F. Bentley, *Appl. Spectrosc.*, 1971, **25**, 155–173.

60 D. Tuschel, *Spectroscopy*, 2015, **30**, 17–22.

61 S. F. Parker, D. Lennon and P. W. Albers, *Appl. Spectrosc.*, 2011, **65**, 1325–1341.

62 K. Drużbicki, J. Mielcarek, A. Kiwilsza, L. Toupet, E. Collet, A. Pajzderska and J. Wąsicki, *Cryst. Growth Des.*, 2015, **15**, 2817–2830.

63 P. J. A. Ribeiro-Claro, P. D. Vaz, M. M. Nolasco and A. M. Amado, *Spectrochim. Acta, Part A*, 2018, **204**, 452–459.

64 L. Zhong and S. F. Parker, *R. Soc. Open Sci.*, 2018, **5**, 181363.

65 P. J. A. Ribeiro-Claro, P. D. Vaz, M. M. Nolasco, C. F. Araujo, F. P. S. C. Gil and A. M. Amado, *Chem. Phys. Lett.*, 2019, **737**, 100006.

66 C. Sándorfy, *J. Mol. Struct.*, 2002, **614**, 365–366.

67 C. Sándorfy, *J. Mol. Struct.*, 2006, **790**, 50–54.

68 E. Vogt, C. Vindahl Jensen and H. G. Kjaergaard, *J. Phys. Chem. A*, 2024, **128**, 392–400.

69 N. Rekik and M. J. Wójcik, *Chem. Phys.*, 2010, **369**, 71–81.

70 C. Puzzarini, J. Bloino, N. Tasinato and V. Barone, *Chem. Rev.*, 2019, **119**, 8131–8191.

71 C. Qu and J. M. Bowman, *Phys. Chem. Chem. Phys.*, 2019, **21**, 3397–3413.

72 S. F. Parker, *ChemPlusChem*, 2024, e202400461.

73 (*a*) CCDC 2385127: Experimental Crystal Structure Determination, 2025, DOI: **10.5517/ccdc.csd.cc2l1xl5**; (*b*) CCDC 2385128: Experimental Crystal Structure Determination, 2025, DOI: **10.5517/ccdc.csd.cc2l1xm6**.

24776 | *Phys. Chem. Chem. Phys.*, 2025, **27**, 24766–24776

This journal is © the Owner Societies 2025